Supporting Information

Enhancing the Water Oxidation Electrocatalysis of Correlated Perovskite Nickelates via Disordering the NiO$_6$ Octahedra

Haifan Li[a,b], Yuzhao Wang[c], Jingxin Gao[a], Vei Wang[d]*, Kaiqi Nie[e], Fanqi Meng[f], Xiaoguang Xu[a], Yong Jiang[a], Nuofu Chen[c], Yifei Sun[g]*, Jikun Chen[a]*

[a] *School of Materials Science and Engineering, University of Science and Technology Beijing, Beijing, 100083, China*

[b] *Department of Chemistry, City University of Hong Kong, Kowloon, 999077, Hong Kong SAR, China*

[c] *School of Renewable Energy, North China Electric Power University, Beijing 102206, China*

[d] *Department of Applied Physics, Xian University of Technology, Xian 710054, China*

[e] *Beijing Synchrotron Radiation Facility, Institute of High Energy Physics, Chinese Academy of Sciences, Beijing 100049, China*

[f] *School of Materials Science and Engineering, Tsinghua University, Beijing 100084, China*

[g] *Shenzhen Research Institute of Xiamen University, Shenzhen 518057, China*

Corresponding authors: Prof. Vei Wang (wangvei@icloud.com), Prof. Yifei Sun (yfsun@xmu.edu.cn), and Prof. Jikun Chen (jikunchen@ustb.edu.cn)

Table of contents

I. Experimental Section

Sample preparation of Sm$_x$Nd$_{1-x}$NiO$_3$/LaAlO$_3$ (001) thin films. Chemical solution deposition (CSD) was adopted to grow Sm$_x$Nd$_{1-x}$NiO$_3$ films on LaAlO$_3$ (001) substrates. Take Sm$_{0.5}$Nd$_{0.5}$NiO$_3$/LaAlO$_3$ (001) thin film as an example, 0.002 mol nickel (II) acetate tetrahydrate (NiC$_4$H$_6$O$_4$·4H$_2$O, 99.9% metals basis, Aladdin), 0.001 mol neodymium (III) nitrate hexahydrate (NdN$_3$O$_9$·6H$_2$O, 99.9% metals basis, Aladdin) and 0.001 mol samarium (III) nitrate hexahydrate (SmN$_3$O$_9$·6H$_2$O, 99.9% metals basis, Aladdin) were used as the solute of the precursor solution, weighing in a molar ratio of Re:Ni = 1:1, while 20 mL 2-methoxyethanol (C$_3$H$_8$O$_2$, AR, Aladdin) acted as the solvent. The compound solution was fully stirred for 3 h with a magnetic stirrer (600 r/min) at room temperature to obtain a green and transparent precursor solution. Afterwards, the precursor solution was dropped on the LaAlO$_3$ (001) substrate drop by drop and between each drop the thin film was deposited by spin coating technology at a speed of 1000 rpm for 10 seconds, and at 4000 rpm for another 30 seconds. After 40 times repeat of this process, the spin-coated samples were subjected to a two-step heat treatment of pyrolysis and annealing. Being baked on the dryer for 90s with the temperature of 175 °C, the samples were put into an annealing furnace with the temperature of 800 °C (heating rate 5°C/min), and the oxygen pressure of 15 MPa for 3 h. After annealing, the sample was cooling naturally and then the samples were washed by ethyl alcohol and 0.1 M KCl solution. For ReNiO$_3$ with different ratio of Sm:Nd, all the processes are the same except changing the molar ration of Sm:Nd when preparing the precursor solution. Through utilizing this preparing method, the composition of ReNiO$_3$ thin films can be controlled easily with the well crystallized interface between ReNiO$_3$ and substrates.

Characterization of crystalline structure and transport properties. The crystalline structure and purity of the prepared samples were characterized by θ-2θ x-ray diffraction (XRD) with a scan rate of 0.02 °·s^{-1} in a 2θ scan ranging from 10 ° to 80 ° using a Bruker (D8, Advance, German) instrument equipped with a Cu-Kα radiation (wave length λ = 1.54056 Å). The scanning transmission electron microscopy (STEM) sample was prepared by utilizing Focused Ion Beam (FIB) and the cross-section morphology was characterized by ARM-200CF (JEOL, Tokyo, Japan) transmission electron microscope accompanied with EELS characterization. For Sm$_x$Nd$_{1-x}$NiO$_3$ thin films except SmNiO$_3$, the resistivity-temperature (ρ-T) tendencies were measured by four-terminal method in physical property measurement system (PPMS) system, while the ρ-T tendency of SmNiO$_3$ was measured by four-terminal method in thermoelectric material test system (CTA).

Synchrotron radiation experiment. The near-edge X-ray absorption fine structure (NEXAFS) experiment was performed at 4B9B beamline (photoelectron spectroscopy experiment station) in Beijing Synchrotron Radiation Facility. The O-K edge and Ni-L_2 edge spectra were collected in total electron yield mode and the energy was calibrated by Au-$4f$ core level at 84.0 eV.

Computational method. We have employed the Vienna Ab Initio Package (VASP)[1,2] to perform all the density functional theory (DFT) calculations. The electron-ion interaction was described using projector augmented wave (PAW) method[3,4] and an energy cutoff of 400 eV

was used for the plane wave basis set. The exchange correlation between electrons was treated with generalized gradient approximation (GGA) in the Perdew-Burke-Ernzerhof (PBE)[5] form coupled with the Hubbard on-site Columbic correction (GGA + U)[6,7]. The value U = 4 eV was set to capture the localized state of the $3d$ electrons. Partial occupancies of the Kohn−Sham orbitals were allowed using the Gaussian smearing method and a width of 0.05 eV. The electronic energy was considered self-consistent when the energy change was smaller than 10^{-7} eV. In geometry optimization, both the shapes and internal structural parameters of pristine perovskite $Sm_xNd_{1-x}NiO_3$ unit cell was fully relaxed until the residual force on each atom is less than 0.01 eV/Å with a 10×10×10 Monkhorst-Pack[8] k-point grid for Brillouin zone sampling. As a representative case, we then use it to construct a $Sm_{0.5}Nd_{0.5}NiO_3(100)$ surface model with p (2×2) periodicity in the X and Y directions and 3 stoichiometric layers in the Z direction separated by a vacuum layer in the depth of 15 Å in order to separate the surface slab from its periodic duplicates. This surface model comprises of 6 Nd, 6 Sm, 12 Ni and 36 O atoms, respectively. During structural optimizations, a 2×2×1 k-point grid in the Brillouin zone was used for k-point sampling, and the bottom one stoichiometric layer was fixed while the top two were allowed to relax. The adsorption energy (E_{ads}) of adsorbate A was defined as:

$$E_{ads} = E_{A/surf} - E_{surf} - E_{A(g)}$$

where $E_{A/surf}$, E_{surf} and $E_{A(g)}$ are the energy of adsorbate A adsorbed on the surface, the energy of clean surface, and the energy of isolated A molecule in a cubic periodic box with a side length of 20 Å and a single k-point for Brillouin zone sampling, respectively. The free energy of a gas phase molecule or an adsorbate on the surface was calculated by the equation $G = E + ZPE - TS$, where E is the total energy, ZPE is the zero-point energy, T is the temperature in kelvin (298.15 K is set here), and S is the entropy. The reported standard hydrogen electrode (SHE) model[9] was adopted in the calculations of Gibbs free energy changes (ΔG) of all reaction steps, which was used to evaluate the reaction barrier. The chemical potential of a proton-electron pair, $\mu(H^+) + \mu(e^-)$, is equal to the half of the chemical potential of one gaseous hydrogen molecule, $1/2\mu(H_2)$, at U = 0 V vs SHE at pH = 0. The effect of the applied potential U was estimated using a simple model (CHE) by Nørskov et al. [9], for all reactions involving a proton-electron transfer by shifting the free energy by $-neU$, where n is the number of electrons in the electrochemical reaction:

$$G_{(U)} = G_{(0)} - neU$$

where $G_{(0)}$ is calculated with $G = E + ZPE - TS$, which is the free energy at $U = 0$ V. The potential limiting steps and the overpotential can be determined for different catalysts by this methodology.

Electrochemical measurement. All the $Sm_xNd_{1-x}NiO_3/LaAlO_3$ (001) thin films were packed up by epoxy (detailed in **Figure S7**) so that only the testing surface was exposed to the electrolyte and the exposing area is approximately 50 mm². All the electrochemical experiments were conducted on a CHI 760E electrochemical workstation (CH Instruments, Inc., Shanghai) with a standard three-electrode system. The 1.0 M KOH were prepared by using the deionized water (18.3 MΩ·cm), KOH (Aladdin, 95%). to achieve high purity. The electrolyte was bubbled with an Ar flow for 30 min before the electrochemical measurement. The as-packed $Sm_xNd_{1-x}NiO_3$ films, Hg/HgO electrode and graphite rod acted as the working electrode, reference

electrode, and counter electrode, respectively. Each sample was subjected to numerous CV cycles at a sweeping rate of 50 mV/s until the samples remained stable to establish a relatively stable electrochemical surface. The measured potential values *vs.* the Hg/HgO reference electrode were converted into the RHE scale by using the following equation at 300 K, $E_{RHE} = E_{(Hg/HgO)} + 0.0592 \cdot pH + E^o_{(Hg/HgO)}$, where E_{RHE} is the converted potential *vs.* RHE, $E_{(Hg/HgO)}$ is the measured potential against the Hg/HgO reference electrode, and $E^o_{(Hg/HgO)}$ is the standard potential of Hg/HgO (KOH, 20%) at 298.15 K, i.e., 0.098 V. The linear-scan voltammetry (LSV) curves of all the samples were performed at a scan rate of 5 mV·s^{-1} from 1.0 V to 0 V *vs.* Hg/HgO. Electrochemical impedance spectroscopy (EIS) was performed for all samples to measure uncompensated resistance (R_s) for *iR* correction and charge-transfer resistance (R_{ct}) in a frequency range from 350000 Hz to 0.1 Hz with an amplitude of 10 mV at 0.7 V *vs.* Hg/HgO. The Chronoamperometry (*i-t*) was performed for $Sm_{0.5}Nd_{0.5}NiO_3/LaAlO_3$ (001) at the current density of 50 mA·cm^{-2} for 100 h in 1.0 M KOH electrolyte. All polarization curves were plotted with *iR* correction based on the formula $E_{iR\,corr} = E_0 - i \times R_s$. The cyclic voltammetry (CV) scans were performed for $Sm_xNd_{1-x}NiO_3/LaAlO_3$ (001) samples in a 0.1 M KOH electrolyte from 0.1 to 0.8 V *vs.* Ag/AgCl at various scan rates ranging from 10 to 100 mV·s^{-1} to quantify the reactivity of lattice oxygen (O_L) by using Lavrion equation and Randles-Savcik equation. Electrochemically active surface area (ECSA) was measured for $Sm_xNd_{1-x}NiO_3/LaAlO_3$ (001) samples from 0.02 to 0.12 V *vs.* Ag/AgCl in 0.1 M KOH. The results of double-layer capacitance (C_{dl}) and ECSA were detailed in **Figure S15-S16**.

TOF calculation. The TOF was calculated to discuss the intrinsic activity of the material according to the equation:

$$TOF = j \cdot A / 4FN$$

where F is the Faraday constant (96485 C·mol^{-1}); N is the mole number of active atoms on the electrode; j is the current density (mA·cm^{-2}) obtained at overpotential (η) = 370 mV vs. RHE, normalized by the working electrode area; A is the geometric area (e.g., 0.5 cm^{-2}). The number of active sites (N) is estimated via the following method[10]:

The active sites per real surface area (N_0) can be calculated by the following equation:

$$N_0 = (\frac{N_{cell}}{V_{cell}})^{2/3}$$

where N_0 is the number of atoms acted as active sites in a unit cell, which can be obtained from the models for DFT calculation as previously shown in Figure S5, V_{cell} is the volume of the untie cell. After the N_0 was calculated, the number of active sites (N) can be calculated according to the equation[11]:

$$N = N_0 \cdot A_{ECSA}$$

where A_{ECSA} is the electrochemically active surface area (ECSA) calculated by double-layer capacitance (C_{dl}) as previously detailed in Figure S14-S15 according to the following equation[11]:

$$A_{ECSA} = A \cdot \frac{C_{dl}}{C_{dl\,ref}}$$

where $C_{dl\,ref}$ is the reference double-layer capacitance and it was previously reported that the

surface double-layer capacitance of ideal smooth oxide is 60 $\mu F \cdot cm^{-2}$.[12] Take $NdNiO_3$ as example, the V_{cell} of $NdNiO_3$ unite cell is 220.613 $Å^3$ while the number of O atoms (the active site) in the unite cell is 12. The oxygen site is the active site in our DFT calculation as proved by Figure 5a thus the N_0 of $NdNiO_3$ was calculated to be 0.1436 $Å^{-2}$. Based on the A_{ECSA} calculated by the C_{dl} in Figure S15, the TOF of $NdNiO_3$ was calculated to be 0.066 s^{-1}. Following the same process, the calculated TOF is listed as follows: $Sm_{0.5}Nd_{0.5}NiO_3$ 0.258 s^{-1}, $Sm_{0.4}Nd_{0.6}NiO_3$ 0.163 s^{-1}, $Sm_{0.25}Nd_{0.75}NiO_3$ 0.102 s^{-1}, $NdNiO_3$ 0.066 s^{-1}, $Sm_{0.6}Nd_{0.4}NiO_3$ 0.084 s^{-1}.

II. The crystalline structures and transport properties for $Sm_xNd_{1-x}NiO_3$

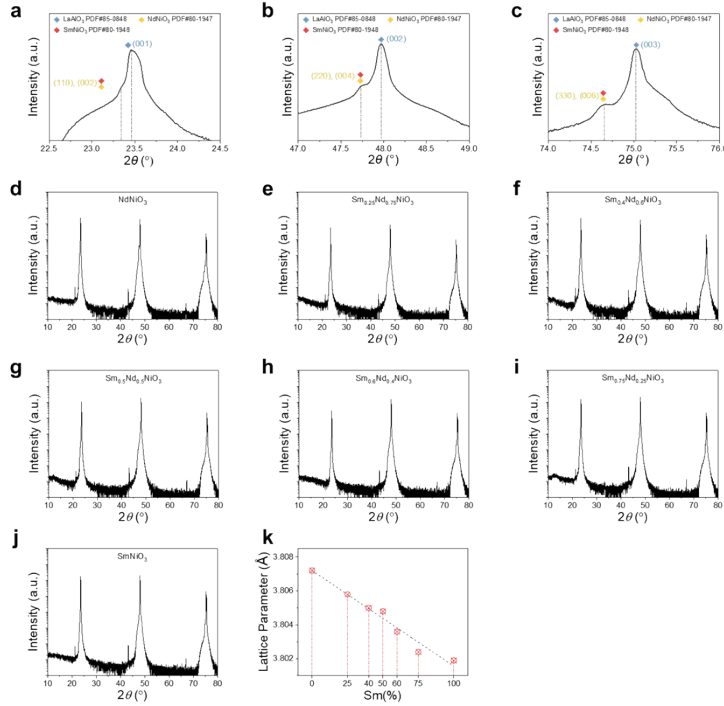**Figure. S1.** (a-c) The local enlarged XRD results of representative $Sm_{0.5}Nd_{0.5}NiO_3/LaAlO_3$ (001). (d-j) The XRD pattern of $Sm_xNd_{1-x}NiO_3/LaAlO_3$ (001) films (x = 0, 0.25, 0.4, 0.5, 0.6, 0.75, 1.0). (k) The calculated interplanar spacing (d) of (002) planes for $Sm_xNd_{1-x}NiO_3/LaAlO_3$ (001) films. The d of (002) planes of these samples were calculated by Bragg diffraction equation as follows:

$$2dsin\theta = n\lambda$$

where θ is the diffraction angle, n = 1, and the wave length λ = 1.54056 Å. Although the ideal structure of perovskite material is cubic system and there is lattice distortion within ReNiO$_3$ materials and the degree of NiO$_6$ distortion depends on the radius of A-site rare earth cations, there is no difference in calculating the lattice parameter c by utilizing the formulations for

calculating d within rhombic system ($\frac{1}{d^2} = \frac{h^2}{a^2} + \frac{k^2}{d^2} + \frac{l^2}{d^2}$) or cubic system ($d^2 = \frac{a^2}{h^2 + k^2 + l^2}$)

for (002) plane and the results are shown in Figure. S1k. With the increasing of Sm%, the degree of the distortion of NiO$_6$ octahedron is larger and the Ni-O-Ni bond angle will gradually decrease, resulting in the weakening of Ni-O hybridization.
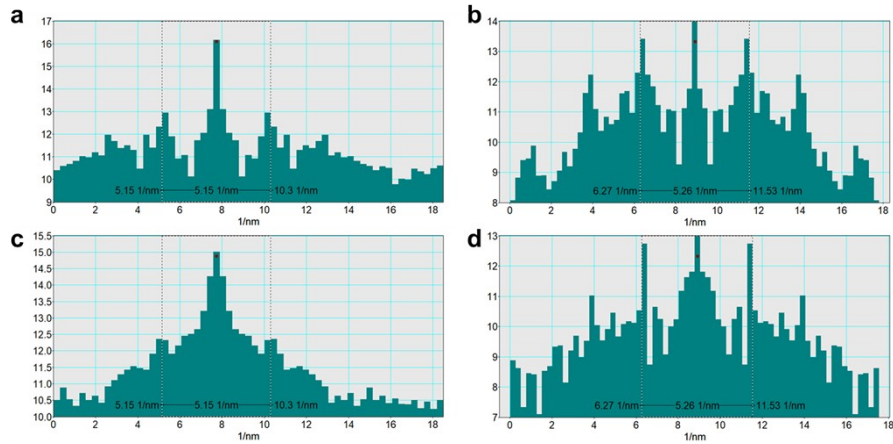
Figure. S2. Calculating the interplanar spacing (d) for the region marked in (a-b) red framework and (c-d) yellow framework, respectively, through Gatan (GMS3, a professional electron microscope data processing software). By measuring the distance (l) between a pair of diffraction spots, the interplanar spacing can be calculated as $d = 2/l$. Therefore, the interplanar spacing corresponds to the diffraction spots in Figure 1d can be calculated as 0.3883 nm and 0.3802 nm, respectively, closer to the d of (110) and (002) planes of $SmNiO_3$ and $NdNiO_3$.
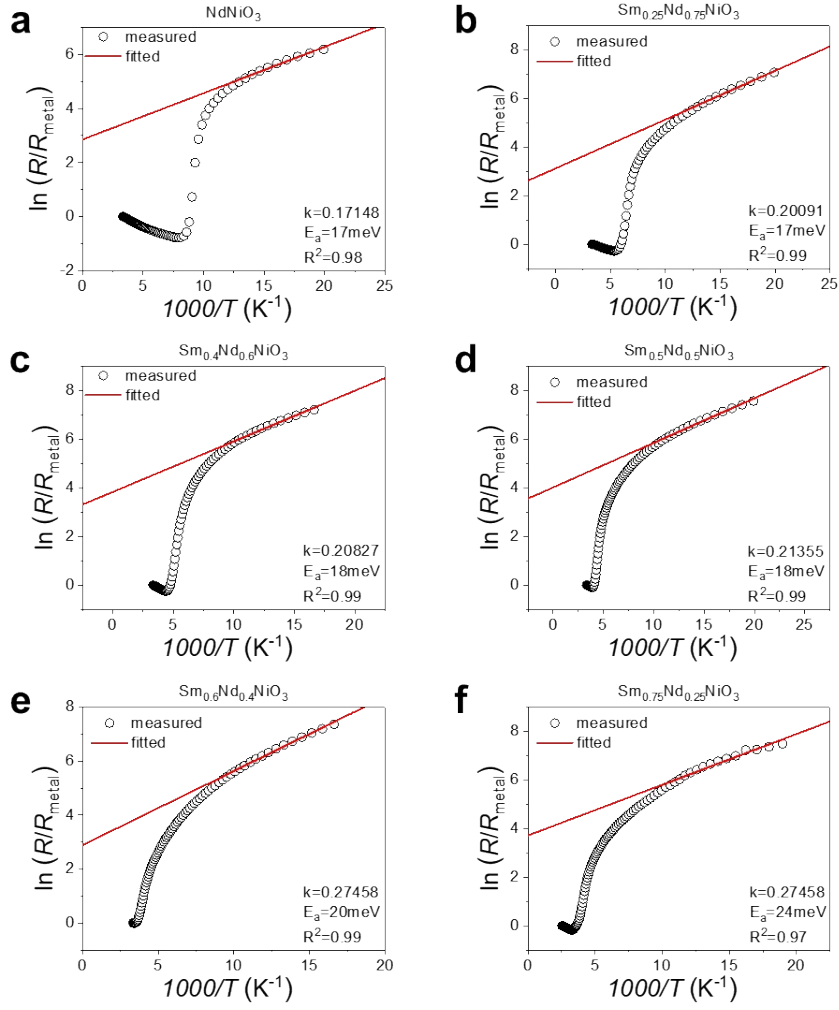
Figure. S3. (a-f) The calculating thermal aviation energy (E_a) of $Sm_xNd_{1-x}NiO_3$/LaAlO$_3$ (001) films (x = 0, 0.25, 0.4, 0.5, 0.6, 0.75) based on the temperature dependent resistance data in Figure. 1c in the main text. The formulation is listed as follows:

$$R = R_{metal} \cdot exp(\frac{E_a}{k_B T})$$

where R is the measured resistance, R_{metal} is the highest metallic resistance, Boltzmann constant k_B = 1.380649×10^{-23} J/K, T is the temperature. The results show that all the magnitude of E_a is 10^1 meV, in agreement with the previous report.[13] With the increasing of Sm%, the E_a gradually increases, corresponding to the less overlapping between conduction band and valence band as illustrated in Figure. 1a.

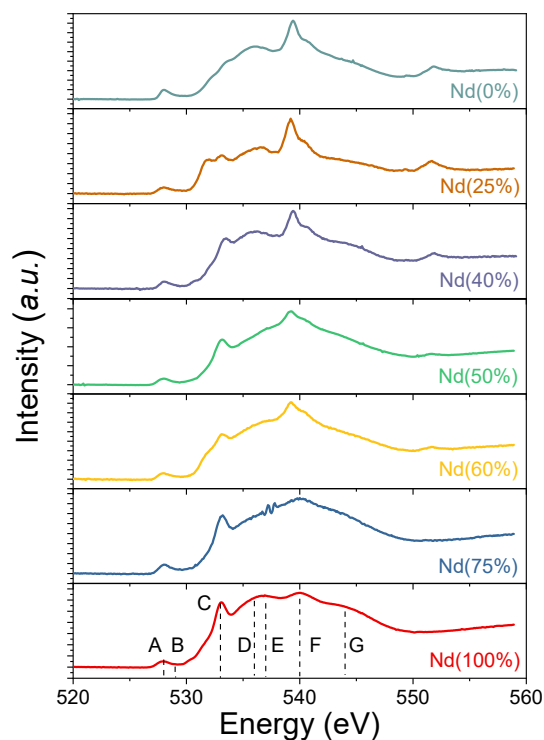**III. The results of NEXAFS and DFT calculations for Sm$_x$Nd$_{1-x}$NiO$_3$.**

Figure. S4. The X-ray absorption near-edge fine structure (XANES) of O-*K* edges for Sm$_x$Nd$_{1-x}$NiO$_3$/LaAlO$_3$ (001) films (*x* = 0, 0.25, 0.4, 0.5, 0.6, 0.75, 1.0). The shape-resonances marked as A-G arise from the following transitions: (A) the pre-peak at about 528 eV associated with the hybridization between Ni-3*d* and O-2*p* orbitals.[14-16] (B) the shoulder peak at about 530 eV attributed to the presence of non-equivalent Ni sites as compared to shape-resonance labelled A.[16-18] (C and D) two broad peaks at about 533 eV and 536 eV, respectively, arise from the hybridization among O-2*p*, *Re*-5*d* and *Re*-4*f* orbitals.[19,20] (E, F and G) the broad peaks originate from the hybridized metal-oxygen orbitals involving Ni-4*sp*, *Re*-5*sp*, and O-2*p* orbitals.[21,22] Therefore, in the main text the integral intensity between two shape-resonances marked as A and B can be calculated to evaluate the degree of hybridization between Ni-3*d* and O-2*p* orbits.
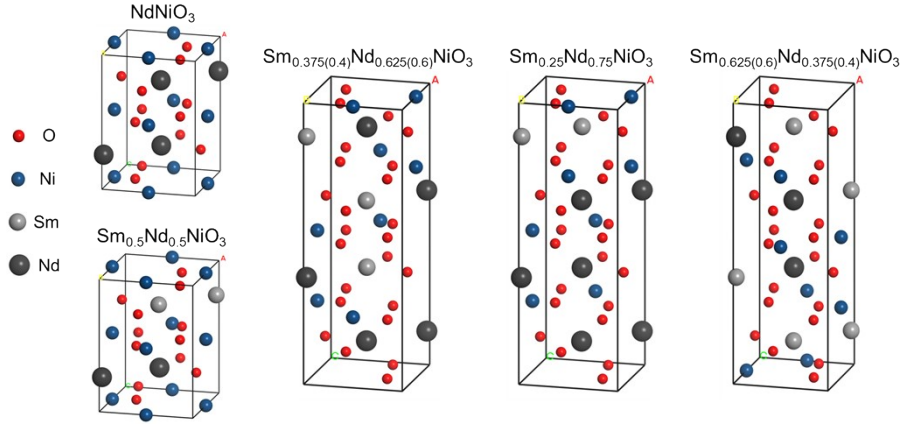
Figure. S5. Ball-and-stick model for $NdNiO_3$ primitive cell and $Sm_xNd_{1-x}NiO_3$ alloys.

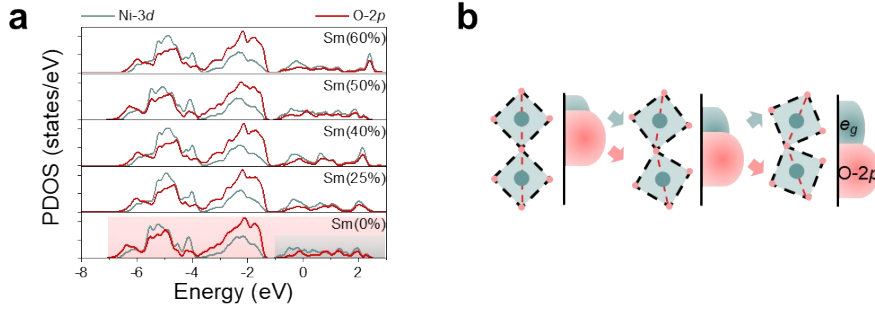**Figure S6.** (a) The partial density of states (PDOS) of $Sm_xNd_{1-x}NiO_3/LaAlO_3$ (001) samples (x = 0, 0.25, 0.4, 0.5, 0.6) calculated by DFT (detailed in methods). (b) Schematic diagram for the simultaneously dynamic changes of the NiO_6 octahedral distortion and the shift of e_g and O-2p band centers. The O-2p and Ni-3d bands all across the Fermi energy (E_F), indicating p-d hybridization, in agreement with the metallic transport behavior at room temperature as also supported by the R-T results. Compared to the results of $Sm_{0.6}Nd_{0.4}NiO_3$ and $Sm_{0.4}Nd_{0.6}NiO_3$, the distribution of DOS for O-2p and Ni-3d bands near E_F in the results of $Sm_{0.5}Nd_{0.5}NiO_3$ are more uniform without shape-resonance at specific energy positions. In addition, the constriction of energy distributing range can be obviously observed in the PDOS results of $Sm_{0.5}Nd_{0.5}NiO_3$, indicating its band shifting toward E_F compared to other cases. The energy range for integration is marked by the color-block for O-2p and e_g bands and the formulations for calculating the energy position of their band centers are listed as follows[23,24]:

$$\varepsilon_{d/p} = \frac{\int_{-\infty}^{+\infty} n_{d/p}(\varepsilon)\varepsilon d\varepsilon}{\int_{-\infty}^{+\infty} n_{d/p}(\varepsilon)d\varepsilon}$$

where $\varepsilon_{d/p}$ is the energy position of the band centers of O-2p or e_g bands, $n_{d/p}(\varepsilon)$ is is the density of states, ε is the energy. Herein, the energy range for integration of O-2p and e_g bands is -7 eV to 3 eV and -1 eV to 3 eV, respectively, and the results are shown in Figure 3c in the main text.

IV. The encapsulation of $Sm_xNd_{1-x}NiO_3$ and their electrochemical activity testing.
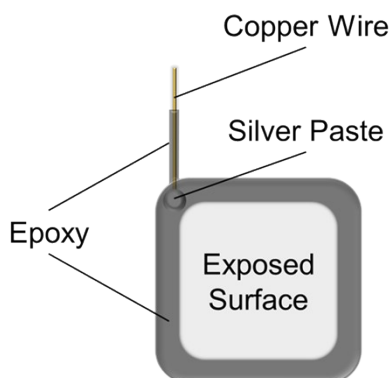

Figure. S7. Schematic diagram for the packing of our samples. All the samples we used were packed up by epoxy to cover the substrates, the copper wire and the silver paste used to connect the films and the conducting wires to avoid interference of signals outside the thin films. The exposing area of our samples is approximately 50 mm^2.
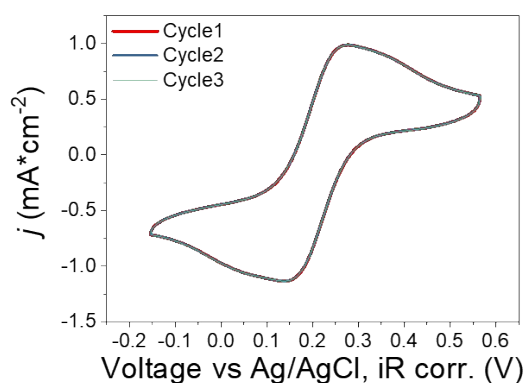

Figure. S8. The cyclic voltammetry (CV) results of $Sm_{0.5}Nd_{0.5}NiO_3/LaAlO_3$ (001) in 5 Mm $K_4[Fe(CN)_6]/K_3[Fe(CN)_6]$ in 0.1M KCl solution at a scan rate of 50 mV·s^{-1}. The symmetric redox peak related to the redox reaction between Fe^{2+}/Fe^{3+} originated at 0.3V and 0.1V vs. Ag/AgCl, respectively, suggesting the reliable transport properties of our samples.
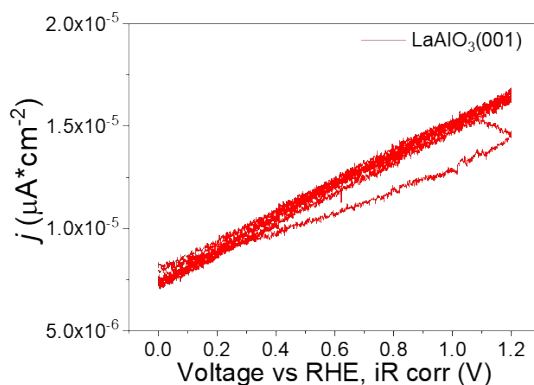

Figure. S9. The linear-scan voltammetry (LSV) curves of the bare substrates at a scan rate of 10 mV·s^{-1} in 0.1 M KOH electrolyte, and the contribution of the $LaAlO_3$ substrates to current density (j) is negligible.

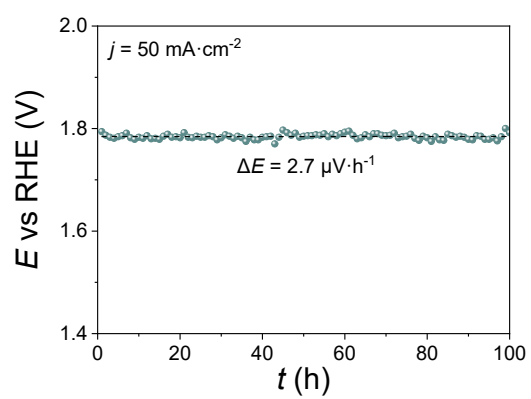**Figure. S10.** The result of chronoamperometry (*i-t*) at 50 mA·cm^{-2} for representative Sm$_{0.5}$Nd$_{0.5}$NiO$_3$/LaAlO$_3$ (001).

Table S1. The comparison of OER activity of various representative oxide electrocatalysts.

| Catalyst	Overpotential (mV) @10 mA·cm^{-2}	Tafel slope (mV·dec^{-1})	Electrolyte (KOH)	Reference
$Sm_{0.5}Nd_{0.5}NiO_3$	340	75	1.0 M	This work
$La_{0.75}Sr_{0.25}Mn_{0.5}Fe_{0.5}O_3$	428	84.3	1.0 M	*Sci. China Mater.*, 2022, 66, 1002
$La_{0.5}Sr_{0.5}Co_{0.8}Cu_{0.2}O_{3-\delta}$	500	60.5	1.0 M	*J. Solid State Chem.*, 2023, 317
$SrCo_{0.95}Si_{0.05}O_{3-\delta}$	410	63	0.1 M	*Int. J. Hydrogen Energy*, 2022, 47, 39108
$Pr_{0.6}Sr_{1.2}FeO_{3-\delta}$	400	64.3	0.1 M	*Electrochim. Acta*, 2022, 430
$La_{0.2}Sr_{0.8}Co_{0.9}Nb_{0.1}O_{3-\delta}$	450	100.8	1.0 M	*Ceram. Int.*, 2022, 48, 36992
$LaSr_3Co_{1.5}Fe_{1.5}O_{10-\delta}$	388	83.9	1.0 M	*Nano Energy*, 2017, 40, 115
$La_{0.5}Sr_{1.5}Ni_{1-x}Fe_xO_{4\pm\delta}$	360	44	0.1 M	*Nat. Commun.*, 2018, 9, 3150
$La_{1-x}Sr_xCo_{1-y}Fe_yO_{3-\delta}$	440	109	1.0 M	*ACS Appl. Energy Mater.*, 2018, 1, 3342
$LaNiO_3$	460	96	1.0 M	*Adv. Ener. Mater.*, 2021, 11, 2003755
$LaCoO_3$	380	N/A	0.1 M	*Adv. Funct. Mater.*, 2021, 31, 2101632
$La_{0.8}Sr_{0.2}Co_{0.8}Ni_{0.2}O_{3-\delta}$	350	85	1.0 M	*Mater. Adv.*, 2022, 3, 272
$La_{0.8}Sr_{0.2}Co_{0.8}Mn_{0.2}O_{3-\delta}$	350	84	1.0 M	*Mater. Adv.*, 2022, 3, 272
$(Co, Cu, Fe, Mn, Ni)_3O_4$	400	76.7	1.0 M	*J. Mater. Chem. A*, 2019, 7, 24211
$K(MgMnFeCoNi)F_3$	397	61	0.1 M	*J. Am. Chem. Soc.*, 2020, 142, 10, 4550
$La_{1.5}Sr_{0.5}NiMn_{0.5}Ru_{0.5}O_6$	430	N/A	0.1 M	*ACS Appl. Mater. Interfaces*, 2019, 11, 21454

V. The verification of OER mechanism for $Sm_xNd_{1-x}NiO_3$.
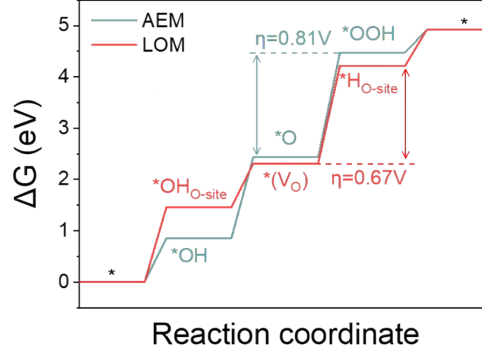
Figure. S11. The equilibrium lattice constant of perovskite $Sm_{0.5}Nd_{0.5}NiO_3$ unit cell was optimized, when using a 10×10×10 Monkhorst-Pack k-point grid for Brillouin zone sampling, to be a=3.767 Å. We then use it to construct a $Nd_{0.5}Sm_{0.5}NiO_3(100)$ surface model with p (2×2) periodicity in the X and Y directions and 3 stoichiometric layers in the Z direction separated by a vacuum layer in the depth of 15 Å in order to separate the surface slab from its periodic duplicates. This surface model comprises of 6 Nd, 6 Sm, 12 Ni and 36 atoms. During structural optimizations, a 2×2×1 k-point grid in the Brillouin zone was used for k-point sampling, and the bottom one stoichiometric layer was fixed while the top two were allowed to relax. The adsorption energy (E_{ads}) of adsorbate A was defined as:

$$E_{ads} = E_{A/surf} - E_{surf} - E_{A(g)}$$

where $E_{A/surf}$, E_{surf} and $E_{A(g)}$ are the energy of adsorbate A adsorbed on the surface, the energy of clean surface, and the energy of isolated A molecule in a cubic periodic box with a side length of 20 Å and a 1×1×1 Monkhorst-Pack k-point grid for Brillouin zone sampling, respectively. The free energy of a gas phase molecule or an adsorbate on the surface was calculated by the equation $G = E + ZPE - TS$, where E is the total energy, ZPE is the zero-point energy, T is the temperature in kelvin (298.15 K is set here), and S is the entropy. The reported standard hydrogen electrode (SHE) model was adopted in the calculations of Gibbs free energy changes (ΔG) of all reaction steps, which was used to evaluate the reaction barrier. The chemical potential of a proton-electron pair, $\mu(H^+) + \mu(e^-)$, is equal to the half of the chemical potential of one gaseous hydrogen molecule, $1/2\mu(H_2)$, at U = 0 V vs SHE at pH = 0.
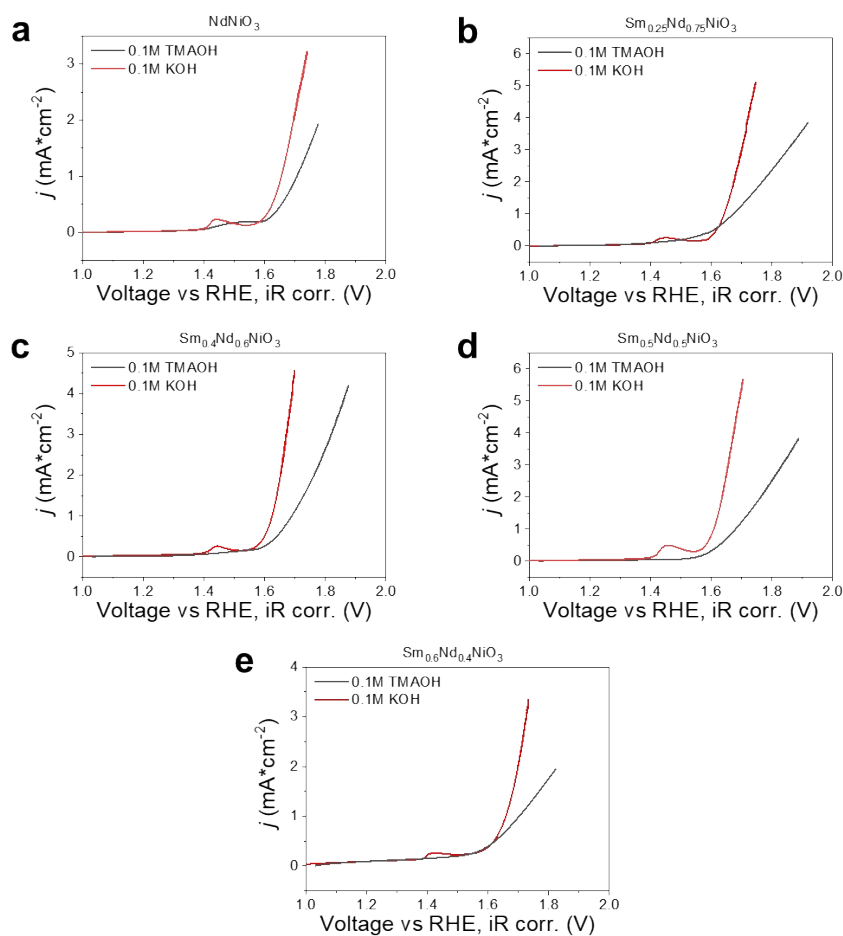
Figure. S12. The linear-scan voltammetry (LSV) results of $Sm_xNd_{1-x}NiO_3/LaAlO_3$ (001) samples ($x = 0, 0.25, 0.4, 0.5, 0.6$) in 0.1 M KOH and 0.1 M TMAOH electrolyte, respectively. The TMA$^+$ group can bind with negative oxygenated intermediates (e.g., O_2^{2-} and O_2^-), inhibiting the surface adsorption of OER intermediate of lattice oxygen mechanism (LOM), thereby reducing its OER catalytic activity. Therefore, the pre-peaks were almost disappeared while performing OER in TMAOH electrolyte and the current density significantly declined.

VI. The quantitative calculation of the diffusion coefficient of O_L for $Sm_xNd_{1-x}NiO_3$.
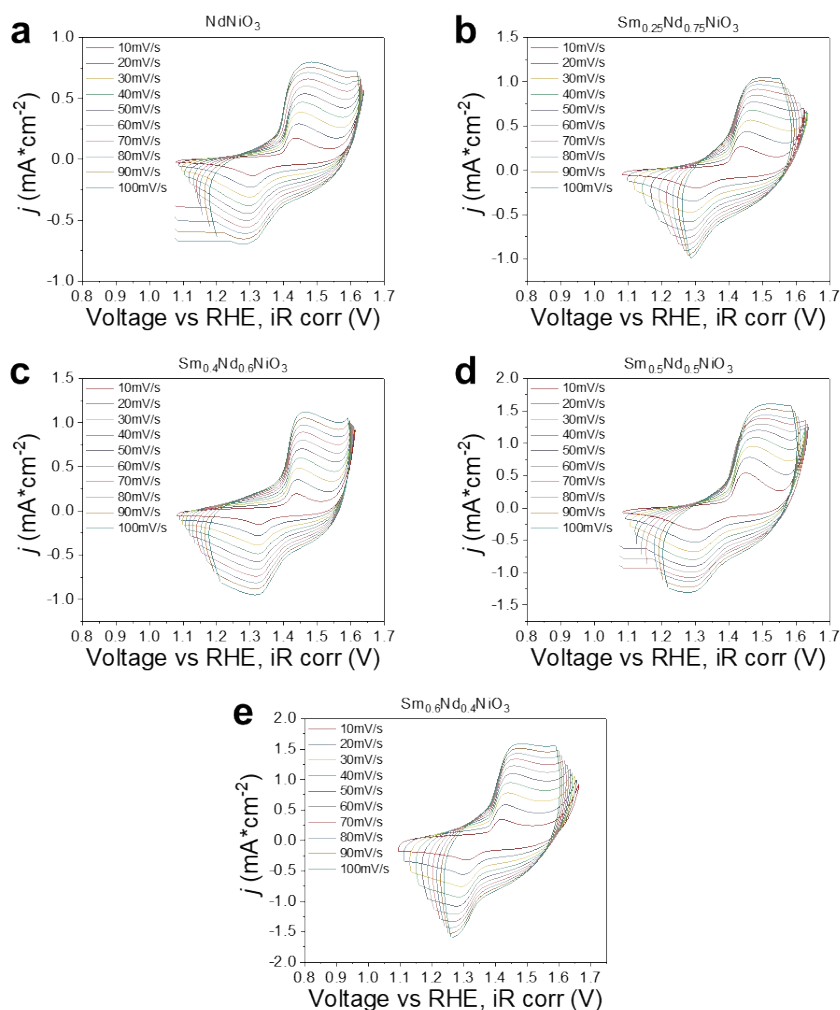

Figure. S13. The cyclic voltammetry (CV) scans for $Sm_xNd_{1-x}NiO_3/LaAlO_3$ (001) samples (x = 0, 0.25, 0.4, 0.5, 0.6) in a 0.1 M KOH electrolyte from 0.1 to 0.8 V vs. Ag/AgCl at various scan rates ranging from 10 to 100 mV·s^{-1}. It can be seen that all of the loops show clear redox reaction of nickel with various valence states (e.g., $Ni^{2+}/Ni^{3+}/Ni^{4+}$) at about 1.46 V. These redox reactions are not strictly reversible but quasi-reversible, which is a prerequisite for using the Lavrion equation listed in the main text.
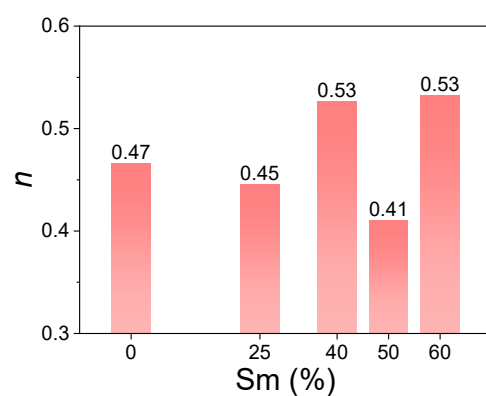
Figure. S14. The number of transferred electrons (*n*) calculated by Lavrion equation:

$$\Delta E_p = E_{pc} - E_{pa} = 2.3\frac{RT}{nF}$$

where E_{pc} and E_{pa} are the potential of cathodic and anodic peak, respectively, R is molar gas constant, T is temperature, and F is faraday constant.

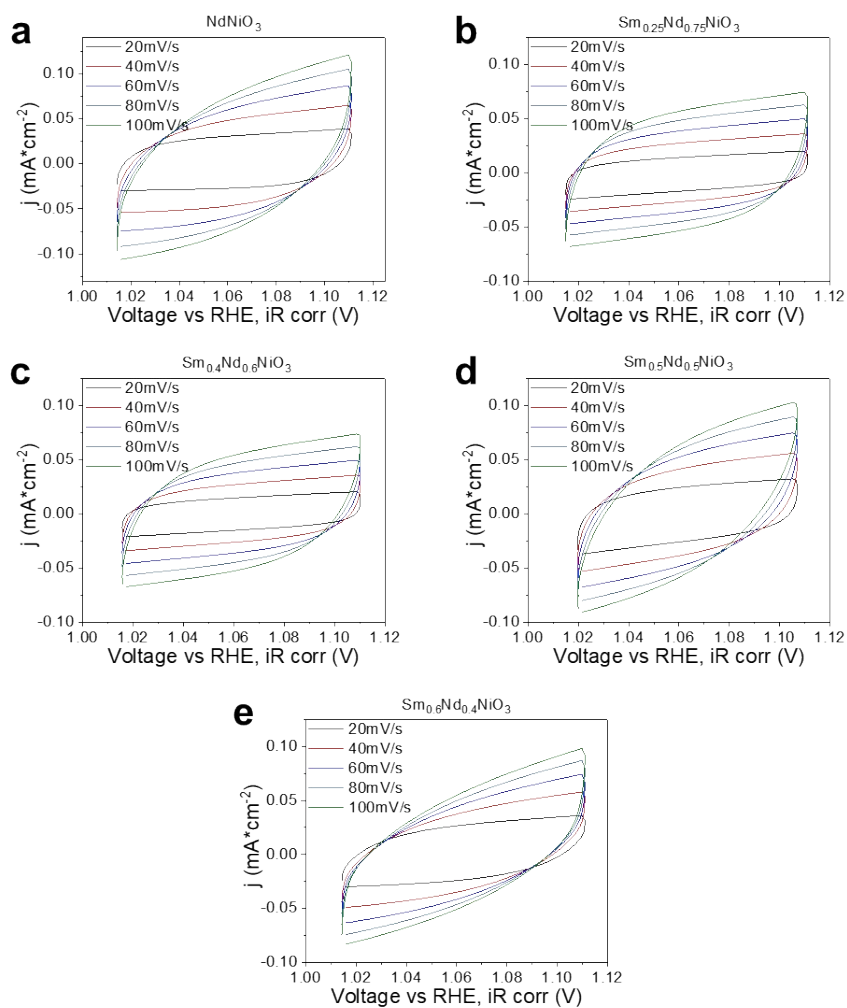# VII The verification of intrinsic OER electrocatalytic activity for $Sm_xNd_{1-x}NiO_3$.

Figure. S15. (a-e) The cyclic voltammetry (CV) scans for $Sm_xNd_{1-x}NiO_3$/LaAlO$_3$ (001) samples (x = 0, 0.25, 0.4, 0.5, 0.6) from 0.02 to 0.12 V vs. Ag/AgCl within 0.1 M KOH.

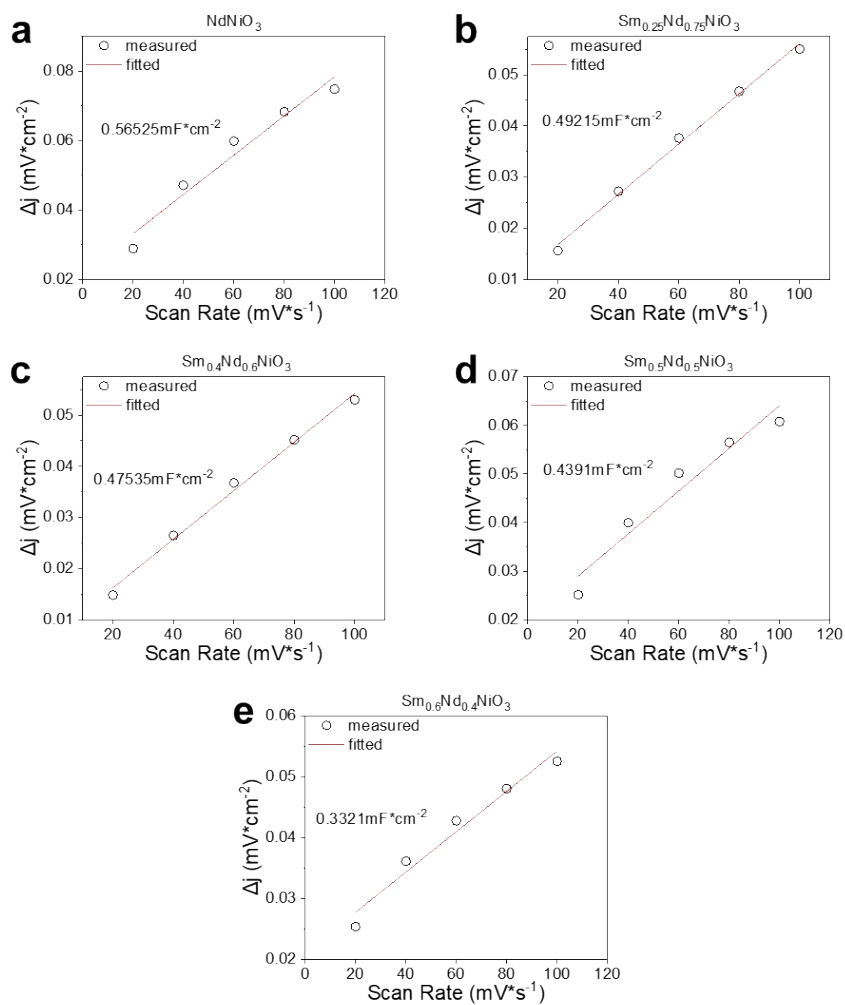**Figure. S16.** (a-e) The linearly fitting of charging current density (Δj) as a function of scan rate for $Sm_xNd_{1-x}NiO_3/LaAlO_3$ (001) samples ($x = 0, 0.25, 0.4, 0.5, 0.6$), where $\Delta j = (j_+ - j_-)/2$ at 1.06 V vs. RHE. The slope of the fitting lines was used for determination of the double-layer capacitance (C_{dl}) in Figure. 7d in the main text.
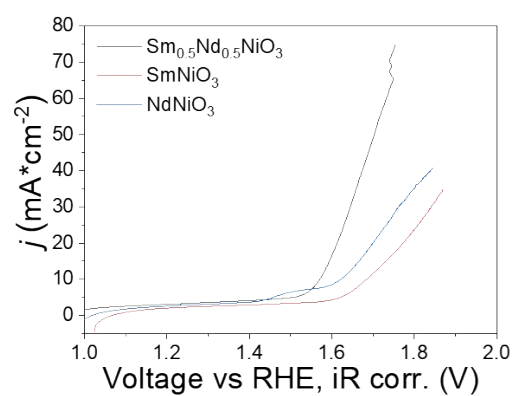
Figure. S17. The LSV results of $Sm_{0.5}Nd_{0.5}NiO_3$, $SmNiO_3$, and $NdNiO_3$ bulks prepared by molten-salt synthesis approach.[25] The result shows that although the preparation technology is changed, the sample with chemical composition as $Sm_{0.5}Nd_{0.5}NiO_3$ performed better than both $SmNiO_3$ and $NdNiO_3$, indicating the intrinsic enhancement of electrocatalysis activity via rare-earth co-occupation strategy.

VII. Reference

(1) Kresse, G.; Furthmüller, J. Efficiency of ab-initio total energy calculations for metals and semiconductors using a plane-wave basis set. *Comp. Mater. Sci.* **1996**, *6*, 15-50.

(2) Kresse, G.; Furthmüller, J. Efficient iterative schemes for ab initio total-energy calculations using a plane-wave basis set. *Phys. Rev. B* **1996**, *54*, 11169-11186.

(3) Kresse, G.; Joubert, D. From ultrasoft pseudopotentials to the projector augmented-wave method. *Phys. Rev. B* **1999**, *59*, 1758-1775.

(4) Blöchl, P. E. Projector augmented-wave method. *Phys. Rev. B* **1994**, *50*, 17953-17979.

(5) Perdew, J. P.; Burke, K.; Ernzerhof, M. Generalized Gradient Approximation Made Simple. *Phys. Rev. Lett.* **1997**, *78*, 1396-1396.

(6) Dudarev, S. L.; Botton, G. A.; Savrasov, S. Y.; Humphreys, C. J.; Sutton, A. P. Electron-energy-loss spectra and the structural stability of nickel oxide: An LSDA+U study. *Phys. Rev. B* **1998**, *57*, 1505-1509.

(7) Vladimir, I. A.; Aryasetiawan, F.; Lichtenstein, A. I. First-principles calculations of the electronic structure and spectra of strongly correlated systems: the LDA+ U method. *J. Phys. Condens. Matter* **1997**, *9*, 767.

(8) Monkhorst, H. J.; Pack, J. D. Special points for Brillouin-zone integrations. *Phys. Rev. B* **1976**, *13*, 5188-5192.

(9) Nørskov, J. K.; Rossmeisl, J.; Logadottir, A.; Lindqvist, L.; Kitchin, J. R.; Bligaard, T.; Jónsson, H. Origin of the Overpotential for Oxygen Reduction at a Fuel-Cell Cathode. *J. Phys. Chem. B* **2004**, *108*, 17886-17892.

(10) Kibsgaard, J.; Jaramillo, T. F. Molybdenum Phosphosulfide: An Active, Acid-Stable, Earth-Abundant Catalyst for the Hydrogen Evolution Reaction. *Angew. Chem., Int. Ed.* **2014**, *53*, 14433-14437.

(11) Voiry, D.; Chhowalla, M.; Gogotsi, Y.; Kotov, N. A.; Li, Y.; Penner, R. M.; Schaak, R. E.; Weiss, P. S. Best Practices for Reporting Electrocatalytic Performance of Nanomaterials. *ACS Nano* **2018**, *12*, 9635-9638.

(12) Chi, B.; Lin, H.; Li, J.; Wang, N.; Yang, J. Comparison of three preparation methods of $NiCo_2O_4$ electrodes. *Int. J. Hydrogen Energ.* **2006**, *31*, 1210-1214.

(13) Shi, J.; Zhou, Y.; Ramanathan, S. Colossal resistance switching and band gap modulation in a perovskite nickelate by electron doping. *Nat. Commun.* **2014**, *5*, 4860.

(14) Kuiper, P.; Kruizinga, G.; Ghijsen, J.; Sawatzky, G. A.; Verweij, H. Character of holes in $Li_xNi_{1-x}O$ and their magnetic behavior. *Phys. Rev. Lett.* **1989**, *62*, 221-224.

(15) Mossanek, R. J. O.; Domínguez-Cañizares, G.; Gutiérrez, A.; Abbate, M.; Díaz-Fernández, D.; Soriano, L. Effects of Ni vacancies and crystallite size on the O 1s and Ni 2p x-ray absorption spectra of nanocrystalline NiO. *J. Phys. Condens. Matter* **2013**, *25*, 495506.

(16) Abbate, M.; Zampieri, G.; Prado, F.; Caneiro, A.; Gonzalez-Calbet, J. M.; Vallet-Regi, M. Electronic structure and metal-insulator transition in $LaNiO_{3-\delta}$. *Phys. Rev. B* **2002**, *65*, 155101.

(17) Scagnoli, V.; Staub, U.; Janousch, M.; Meijer, G. I.; Paolasini, L.; D'Acapito, F.; Bednorz, J. G.; Allenspach, R. Charge disproportionation observed by resonant X-ray scattering at the metal–insulator transition in $NdNiO_3$. *Journal of Magnetism and Magnetic Materials* **2004**, *272-276*, 420-421.

(18) Hayward, M. A.; Rosseinsky, M. J. Synthesis of the infinite layer Ni(I) phase $NdNiO_{2+x}$ by low temperature reduction of $NdNiO_3$ with sodium hydride. *Solid State Sciences* **2003**, *5*, 839-850.

(19) Medarde, M.; Fontaine, A.; García-Muñoz, J. L.; Rodríguez-Carvajal, J.; de Santis, M.; Sacchi, M.; Rossi, G.; Lacorre, P. $RNiO_3$ perovskites (R = Pr, Nd): Nickel valence and the metal-insulator

transition investigated by x-ray-absorption spectroscopy. *Phys. Rev. B* **1992**, *46*, 14975-14984.

(20) Alexander, M.; Romberg, H.; Nücker, N.; Adelmann, P.; Fink, J.; Markert, J. T.; Maple, M. B.; Uchida, S.; Takagi, H.; Tokura, Y.; James, A. C. W. P.; Murphy, D. W. Electronic structure studies on the n-type doped superconductors $R_{2-x}M_xCuO_{4-\delta}$ (R=Pr,Nd,Sm; M=Ce,Th) and $Nd_2CuO_{4-x}F_x$ by electron-energy-loss spectroscopy. *Phys. Rev. B* **1991**, *43*, 333-343.

(21) Bashir, A.; Ikram, M.; Kumar, R.; Thakur, P.; Chae, K. H.; Choi, W. K.; Reddy, V. R. Structural, magnetic and electronic structure studies of $NdFe_{1-x}Ni_xO_3$ ($0 \leq x \leq 0.3$). *J. Phys. Condens. Matter* **2009**, *21*, 325501.

(22) Finazzi, M.; Brookes, N. B. Resonant Auger spectroscopy at the O K edge of NiO. *Phys. Rev. B* **1999**, *60*, 5354-5358.

(23) Hammer, B.; Norskov, J. K. Why gold is the noblest of all the metals. *Nature* **1995**, *376*, 238-240.

(24) Hammer, B.; Nørskov, J. K. Electronic factors determining the reactivity of metal surfaces. *Surface Science* **1995**, *343*, 211-220.

(25) Li, Z. A.; Yan, F. B.; Li, X. Y.; Cui, Y. C.; Wang, V.; Wang, J. O.; Liu, C.; Jiang, Y.; Chen, N. F.; Chen, J. K. Molten-salt synthesis of rare-earth nickelate electronic transition semiconductors at medium high metastability. *Scripta Mater.* **2022**, *207*, 114271.